

Evidence for violations of Weak Cosmic Censorship in black hole collisions in higher dimensions

Tomas Andrade,^a Pau Figueras^b Ulrich Sperhake^{c,d}

^a*Departament de Física Quàntica i Astrofísica, Institut de Ciències del Cosmos, Universitat de Barcelona, Martí i Franquès 1, 08028 Barcelona, Spain*

^b*School of Mathematical Sciences, Queen Mary University of London, Mile End Road, London E1 4NS, United Kingdom*

^c*DAMTP, Centre for Mathematical Sciences, University of Cambridge, Wilberforce Road, Cambridge CB3 0WA, UK*

^d*California Institute of Technology, Pasadena, California 91125, USA*

E-mail: tandrade@icc.ub.edu, p.figueras@qmul.ac.uk,
U.Sperhake@damtp.cam.ac.uk

ABSTRACT: We study collisions of boosted rotating black holes in $D = 6$ and 7 spacetime dimensions with a non-zero impact parameter. We find that there exists an open set of initial conditions such that the intermediate state of the collision is a black hole with a dumbbell-like horizon which is unstable to a local Gregory-Laflamme-type instability. We are able to provide convincing numerical evidence that the evolution of such an instability leads to a pinch off of the horizon in finite asymptotic time thus forming a naked singularity, as in similar unstable black holes. Since the black holes in the initial state are stable, this is the first genuinely generic evidence for the violation of the Weak Cosmic Censorship Conjecture in higher dimensional asymptotically flat spacetimes.

Contents

1	Introduction	1
2	Numerical methods	4
3	Apparent horizons and contours of χ	5
4	Results	8
4.1	$D = 7$	8
4.1.1	Geometry of the AH	8
4.1.2	Gravitational radiation	9
4.2	$D = 6$	13
5	Discussion	14
A	Initial data	17
B	Gravitational waves in 7D	18
C	Radiation peak due to separation	21
D	Radiated energy and angular momentum	22
E	Numerical tests	23

1 Introduction

General Relativity (GR) governs the large scale structure of our Universe. Despite its enormous success, the fact that singularities can be generically formed in dynamical settings [1] in principle calls into question its predictive power. Motivated by this, Penrose postulated the “Weak Cosmic Censorship (WCC) Conjecture” [2], which proposes that singularities formed in dynamical evolution must be hidden inside black hole (BH) horizons. This constitutes a key link between the singularity theorems and the ubiquitousness of astrophysical black holes, for which Penrose was recently awarded the Nobel prize. Through active investigation in over half a century, counter-examples to WCC in settings beyond astrophysics have been found, which can be regarded as a possibility to access the quantum regime of gravity, at least theoretically. They fall into two major categories: i) critical collapse, which involves fine tuning of initial data such that a zero mass singularity is formed in $4D$ and above [3]; ii) death by fragmentation, which results from elongated horizons becoming unstable and eventually pinching off in finite time. The latter category will be the main focus of this article.

The instability which drives the initial stages of this phenomenon was famously discovered by Gregory and Laflamme (GL) [4], who showed, in $5D$ and above, that thin enough black strings (and p -branes in general) have exponentially growing linear modes that trigger spatial modulation along the horizon, in a way that resembles the Rayleigh instability in fluids [5, 6]. Later on, [7, 8] used numerical relativity to follow the unstable black string into the non-linear regime and provided convincing evidence in favour of the pinching off of the horizon in finite time. Moreover, the authors observed the formation of BH satellites joined by thin necks organized in a fractal structure. It is by now understood that not only strings, but all elongated horizons which are locally string (or brane)-like and thin enough, present these unstable modes, e.g., black rings [9], and ultra-spinning BHs [10–15]. The full non-linear evolution of such unstable configurations has been studied in [16–18]. In Refs. [7, 8, 16–18] the quantity that is used to track the shape of the horizon is in fact the apparent horizon. This is justified in view of the quasi-stationary evolution of most of the geometry after the first generation of satellites has formed, which in turn implies that the event horizon is well approximated by the apparent horizon almost everywhere. Even though none of these studies addresses the pinch off of the event horizon and the completeness of future null infinity, it is clear that during the evolution of the GL instability, arbitrarily large curvatures become visible for asymptotic observers in finite time, thus violating at least the spirit of the WCC.

All of the above setups have in common that the starting point is an unstable configuration. Therefore, one may wonder if the so-obtained singularities are a truly generic feature of the evolution in GR. Along these lines, a new and truly generic mechanism for violation of WCC has recently been proposed [19, 20]: the collision of BHs in higher dimensions. The authors of these papers noted that if the total angular momentum is large enough, an elongated horizon should form as an intermediate, long-lived, state after the collision. After this point, the horizon could undergo the breaking described above, depending on the competition between radiation of mass and angular momentum, and the GL instability. The former tends to make the horizon rounder and shorter, thus taming the effect of GL. Since radiation is exponentially suppressed with D and the growth rates of the GL instability remain relatively constant, this mechanism is guaranteed to work if D is sufficiently large. On the other hand, this behaviour is absent in head-on collisions in four or higher dimensions [21, 22], and in grazing BH collisions in 4D [23], none of which exhibit elongated horizons or any signs of censorship violation even when colliding above 90% of the speed of light. Uncovering exactly when and how the proposed phenomenon takes place, requires fully-fledged numerical GR techniques. We note that bar mode instabilities of rotating black holes are known to exist in $6D$ and above [14, 15], so elongated horizons are more likely to exist in $D \geq 6$. For a sufficiently large initial angular momentum, these unstable ‘bar-shaped’ black holes develop a local GL instability. During the evolution of this instability, only about 5% of the total mass of the system is radiated, which is insufficient to prevent the formation of a naked singularity in finite time [18]. Furthermore, Ref. [22] reports that for $v \leq 0.6$, the radiation emitted in head-on collisions is below 1%. All of this considered, we envision that intermediate velocities, relatively high intrinsic spins and impact parameters, and $D \geq 6$ constitute a favourable region for WCC

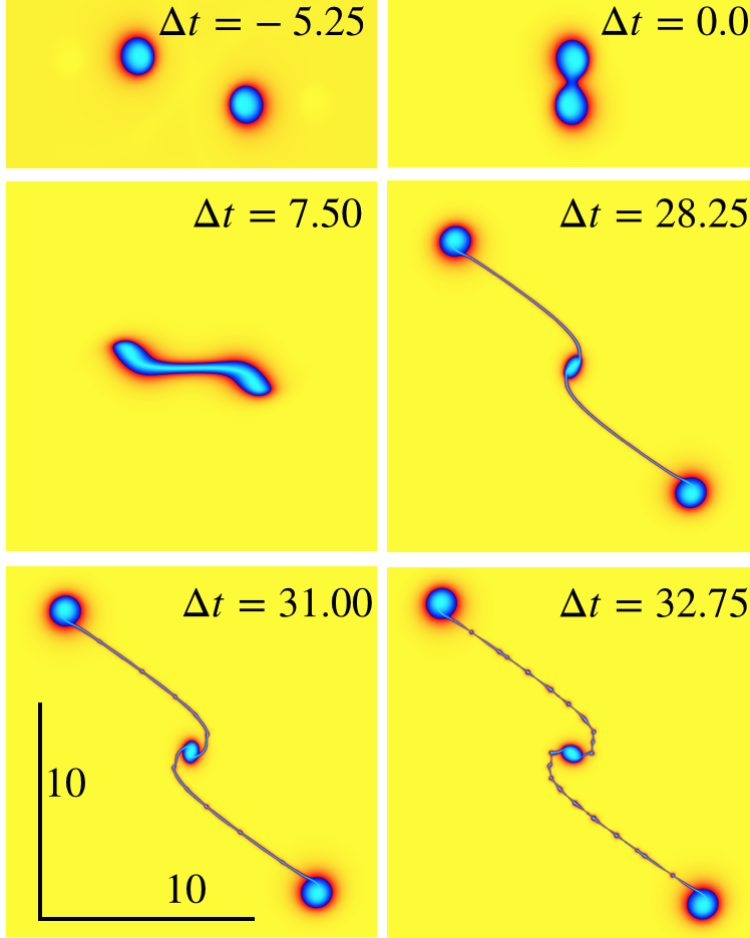


Figure 1: Snapshots of the $7D$ evolution with collision velocity $v = 0.5$, dimensionless spin $a = 0.7$, and impact parameter $b = 2.2$, at times $\Delta t = t - t_{\text{merger}}$. They correspond to: initial condition, merger, bar formation, first generation, second generation, latest stage. We show a spatial length of 10 units on the bottom left panel.

violation in parameter space.

Here we undertake the task of numerically simulating the grazing collision of $6D$ and $7D$ stable, single-spinning BHs with a finite impact parameter. This initial setting is closely analogous to that of a BH binary merger in $4D$, but the spacetime dimensionality gives rise to striking differences in the evolution as we illustrate in Fig. 1 for a specific collision in $7D$. All our simulations start with two separate equal-mass BHs with spin parameter a , collision velocity v and impact parameter b ; cf. the first (upper left) panel in Fig. 1. Over a significant portion of the parameter space, we find that these configurations to form an elongated horizon shortly after merger (second and third panels in the figure). The resulting “neck” grows ever thinner (fourth panel) and breaks through the further evolution of multiple generations of local GL instabilities along the individual string segments (fifth and sixth panel). This process does not require any fine tuning. Moreover, we observe that the late time dynamics resemble the end point of the GL instabilities of black strings

and ultra-spinning BHs of [16–18]. In particular, we observe the formation of two well-defined generations of satellites, and the beginning of a third one. Each generation consists of spherical blobs joined by thin tubes, which can be approximated by quasi-stationary BHs and black strings, respectively. The last stage to which we have access to consists of a central rotating black object, joined by a thin horizon to two non-spinning blobs that move away from each other, see Fig 1; the animation for the full time range covered in our numerics is available at [24]. The thin tubes in the middle are stretching due to the motion of the outer blobs, and develop their own satellites due to their own local GL instabilities. Hence, it is clear that the process will continue until the pinch off, which will take place in finite asymptotic time.

We extract the gravitational waves produced in the collision, finding that the waveforms exhibit two salient peaks. The first one is simply due to the initial merger of the BHs. The second peak produces a stronger signal, and we attribute it to the sudden change of angular velocity and shape of the elongated horizon. Employing a toy model of a $D > 4$ dimensional binary which undergoes a qualitatively similar change in angular velocity and separation, we extract the radiated energy and observe a similar peak; see Appendix C. We find that the total radiated energy is strongly suppressed (it amounts to less than 1% in 7D), confirming the hypothesis that there is no mechanism to stop the formation of a naked singularity in finite asymptotic time.

The organization of the rest of the paper is as follows: In Section 2 we describe the numerical methods that we have used in this paper. Section 3 discussed the relation between the apparent horizon and the contours of the conformal factor χ in the moving punctures gauge that we use. We present our main results for BH collisions in $6D$ and $7D$ in Section 4. We close with a discussion of our results and possible directions for future research in Section 5. We have relegated some technical results to several appendices.

2 Numerical methods

We solve the vacuum Einstein equations in $D = 6, 7$ using the CCZ4 formulation as described in [25, 26]. We restrict ourselves to dynamics in 3+1 dimensions by imposing an $SO(D - 3)$ symmetry by means of the modified cartoon method [14, 27, 28]. The conventions for the damping parameters κ_1 and κ_2 , and choice of gauge evolution are those of Ref. [18]. We construct the initial data by superimposing two boosted Myers-Perry (MP) BHs [29] written in Kerr-Schild (KS) coordinates, as described in Ref. [30]. This yields a mild violation of the constraints on the initial data surface, but in higher dimensions the effect is small for sufficiently separated initial black holes; see Appendix A for details. Henceforth, we split the coordinates as t, x, y, z, w_i where ∂_{w_i} are “cartoon” directions in the language of [28], and choose a single spin aligned with the z -axis.

Without loss of generality, we place one of the BHs at $(x_0, y_0, 0)$ and give it an initial velocity along the x -direction, which we denote by v . We ease the tracking of the dynamics by choosing symmetric data in which the second BH is positioned at $(-x_0, -y_0, 0)$ with speed $(-v, 0, 0)$, which gives an orbital angular momentum pointing in the z -direction. Both black holes have intrinsic spin along the z -direction, with spin parameter a . We

emphasise that in our setting the orbital and intrinsic angular momenta are aligned, which allows us to achieve higher values of the total angular momentum. The impact parameter is controlled by y_0 . Recall that in $D > 4$ there is no inspiral phase in binaries [31], which means that, generically, BHs interact only if y_0 is sufficiently small. While x_0 does not play a fundamental role, we need to choose it such that the initial BHs are sufficiently far apart so that the constraint violations on the initial surface as a result of simply superposing two MP BHs are small. In addition, having a sufficiently large x_0 allows us to decouple the initial gauge dynamics from the collision; our gauge conditions result in an adjustment phase lasting about $\sim 3\mu^{1/(D-3)}$.

We implement the numerical scheme in GRChombo [32, 33], using up to twelve levels of refinement with a 2:1 refinement ratio. We add the extra levels to better resolve the spatial gradients thus keeping the regions of constraint violations far away from the $\chi = 0.6$ surface, which we use as a proxy for the apparent horizon (AH). Here $\chi = (\det \gamma)^{-\frac{1}{3}}$ is the conformal factor, where γ_{ij} is the induced metric on the spatial slices. Recall that χ is one of the evolution variables in the CCZ4 formulation of the Einstein equations; we discuss in detail the relation between the level sets of this variable and the AH in the next section. We have checked the robustness of our results by introducing refinement levels at different times, provided that the extra levels are added whilst the region with constraint violations is sufficiently small. Following [16–18], we apply artificial diffusion in the region $\chi \leq 0.075$ to keep the constraint violations under control. Our computational domain, boundary conditions and time evolution scheme are described in [18]. Finally, we extract the gravitational waves produced in the collisions following Ref. [18]; see Appendix B for details on the wave extraction procedure.

3 Apparent horizons and contours of χ

Our main observables of interest are the location of the AH and the Kretschmann curvature scalar. In our setting, tracking the AH from first principles entails solving a non-linear PDE in two variables at a given instant of time. Shortly after the collision of the two BHs, the common AH evolves into a non-star-shaped surface, with increasingly complex structure as shown in Figs. 1, 9, 10 there exist as yet no algorithms to find the AH for such surfaces.

In this paper, we bypass this difficulty as follows. Reference [18] provides convincing evidence in a variety of scenarios that, in the standard moving punctures gauge, the location of the AH matches within a few percent with a contour of the conformal factor χ . While there is some dependence on the space-time dimension D , this has been observed to be mild [16–18]. Motivated by this, below we will provide quantitative evidence that, for the non-linear evolution of the GL instability in the cases discussed in this paper, the $\chi = 0.6$ contour should accurately track the location of the “apparent horizon”. In particular, this contour should capture the essential features of the AH’s shape. Other contours, such as $\chi = 0.5$ or $\chi = 0.4$, would be comparatively informative. This insensitivity to the specific value of the contour of χ as long as it is sufficiently close to the AH, is due to the steep gradients near the AH of the spacetime metric components in higher-dimensions.

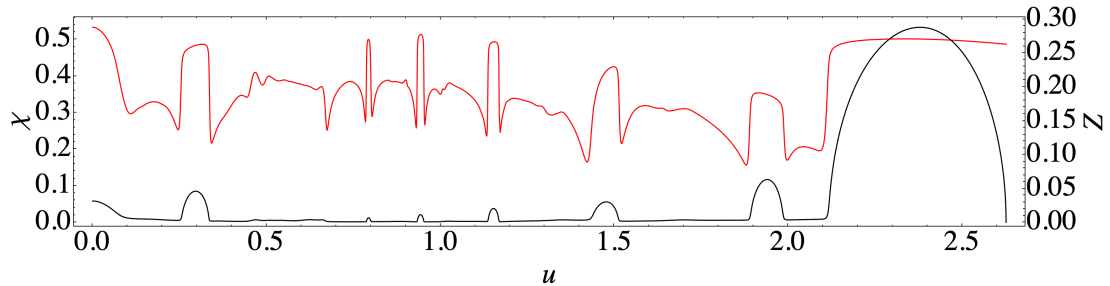


Figure 2: χ (in red) on the AH plotted against the embedding coordinate u near the endpoint of the ultraspinning instability of a MP BH in $6D$ with an initial spin parameter $a/\mu^{1/3} = 1.85$ (see [17] for more details); the Z coordinate of the embedding is shown in black and it serves to guide the eye. This figure shows that on the AH, $\chi \sim 0.5$ on the blobs and $\chi \sim 0.3$ on the necks

As pointed out above, the fact that the AH that forms in the collisions that we study in this article (see Figs. 1, 9, 10), is a non-star-shaped, highly complex and rapidly changing surface, makes the problem of finding it particularly challenging. One possible way forward is to consider a reference surface with the approximate shape of the AH [34, 35]. However, in our case, the reference surface should capture some of the key features that appear as a consequence of the GL cascade; since the latter develops randomly on different scales, both in time and space, finding a suitable reference surface at each time step seems impractical. Alternatively, one could use an intrinsic parametrization of the surface and impose some gauge condition (e.g., harmonic) to fix the reparametrization freedom as in [17]. However, in this reference it was found that the resulting system of equations is not very robust in practice in spite of being manifestly elliptic. Therefore, the problem of parametrizing and finding the AHs that generically appear in higher dimensional BH physics remains open. As we will explain below, a promising avenue would be to use certain contours of the evolved variable χ as the reference surface. This approach has the advantage that these contours capture some of the key features of the AH at any given instant of time and they are readily available since χ is one of the evolved variables. Implementing this in practice is beyond the scope of this article and we leave it for future work.¹

In Fig. 2 we show the values of χ on the AH near the endpoint of the ultraspinning instability of a MP BH in $6D$ with an initial spin parameter $a/\mu^{1/3} = 1.85$ reported by one of us in [17]. The shape of the AH is shown in black. This plot shows that the $\chi = 0.5$ contours capture the ‘bulges’ quite accurately, especially those from the early generations that have reached a quasi-stationary state. On the other hand, the $\chi = 0.3$ contours capture the neck regions of the AH. In Fig. 3 we depict the AH together with different χ contours at some instant of time during the evolution of the GL instability of a black

¹Note that parametrizing a $\chi = \text{const.}$ hypersurface in an efficient and practical way remains challenging because these surfaces are not star-shaped in general.

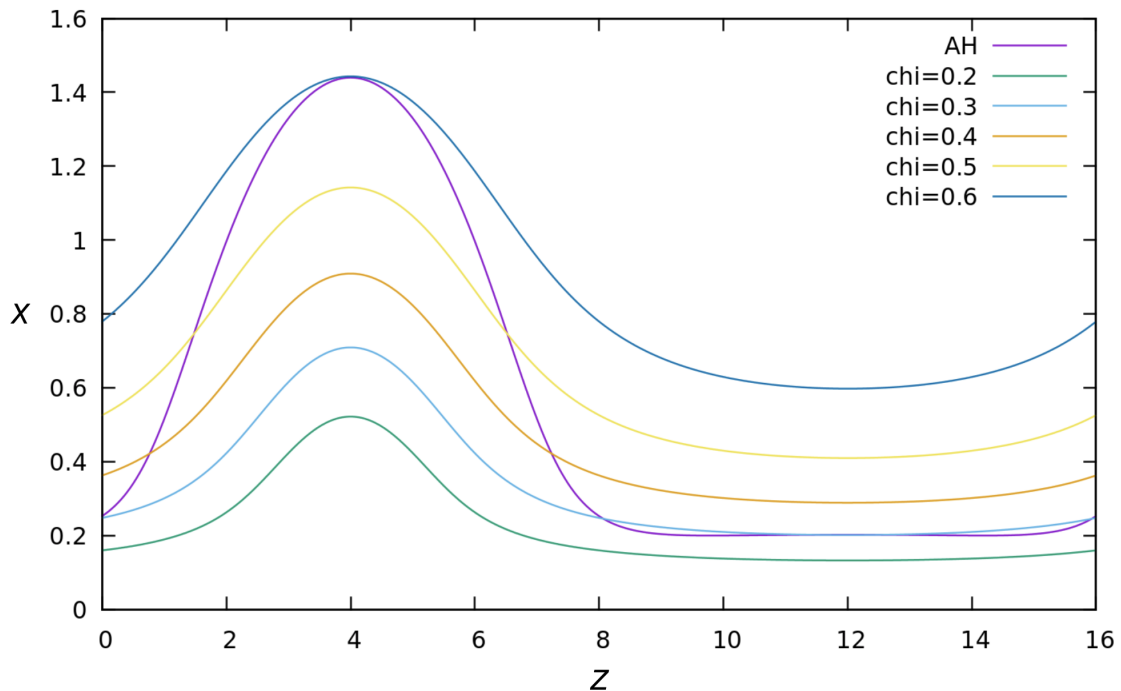


Figure 3: AH and several χ contours during the evolution of the GL instability of a black string in 5D. Here X and Z are the coordinates of the computational domain for a black string with a four-dimensional mass parameter $M = 1$ and a Kaluza-Klein circle with asymptotic length $L = 16$.

string in 5D.² This plot shows that indeed these contours of χ capture the key features of the AH in the evolution of the GL instability, in this case of a black string.

To get some further intuition about which contours accurately describe different portions of the AH during the GL cascade in a BH collision in $D \geq 6$, we evaluate the normalized Kretschmann invariant on a certain χ contour and compare its value to that on the horizon of a stationary black string and a spherical black hole. More precisely, we use the definition

$$\tilde{K} = \frac{1}{240} R^{\alpha\beta\mu\nu} R_{\alpha\beta\mu\nu} W(\chi_0)^4 \quad (3.1)$$

where W is the proper width of a given $\chi = \chi_0$ contour. The normalization in (3.1) has been chosen so that in 7D, $\tilde{K} = 1$ and $\frac{5}{2}$, respectively, on the horizons of stationary black string and a Schwarzschild black hole.

Fig. 4 shows that for the regions of the geometry that have reached a quasi-stationary state, $\tilde{K} \sim 1$ on a $\chi = 0.6$ contour and $\tilde{K} \sim \frac{5}{2}$ on a $\chi = 0.7$ contour. This observation tells us two things: 1) The neck and bulge regions of the AH that have reached a quasi-stationary state are very well approximated by static black strings and spherical black holes respectively, 2) The constant χ contours accurately capture the AH on these regions. Following these observations, it seems justified to use the constant χ contours to track the

²We would like to thank Tiago França and Chenxia Gu for kindly sharing their data with us.

thinning of the neck in the string-like regions and the contour to estimate the masses and angular momenta of the large bulges when we compute the total energy radiated in the collision and subsequent evolution of the system, as we describe in Appendix D.

We should emphasise that this argument of comparing Eq. (3.1) to the value of the Kretschmann scalar on the horizon of a black string or a spherical black hole is only valid if the portion of the horizon that one is considering has reached a quasi-stationary state; on the other hand, there is no reason why the constant χ contours should track the AH in the highly dynamical regions.

4 Results

For both $D = 6, 7$ we have explored the space of parameters a, v, y_0 by running some low resolution simulations until we observe the formation of a long bar-like horizon after the merger. As mentioned in the Introduction, no fine tuning is required in order to achieve such states. Out of the parameters explored, we have selected three study cases to continue the evolution further with the aid of higher resolution simulations. Henceforth we measure time and distance in dimensionless form using the mass parameter μ of a single member of our BH binary. Specifically, we display time in the form of $t = \tilde{t}/\mu^{1/(D-3)}$, where \tilde{t} is coordinate time in geometric units, and likewise for radius r and the Cartesian coordinates x, y, z .

4.1 $D = 7$

The $D = 7$ collision that we have already discussed in the Introduction (Sec. 1), is characterized by initial data with parameters $v = 0.5, a = 0.7, y_0 = 1.1, x_0 = 10$. Note that the spin is within the stability bound $a_{\max} = 0.74$ reported in [15]. First, we have performed a simulation in a small domain of cubic size $L = 64$, including up to 10 levels. In a second stage, to extract the gravitational waves emitted, we repeated the simulation on a domain with size $L = 256$ while keeping the same resolution in the inner levels as in the previous run.

4.1.1 Geometry of the AH

The time evolution obtained in our 7D simulation is displayed in Fig. 1 above, which clearly shows that a dumbbell-shaped horizon forms after merger, consisting of two spherical blobs joined by a thin neck. Moreover, we observe the appearance of spatial modulation along the horizon, characteristic of the GL instability. At the same time, the length of the dumbbell increases making the middle neck thinner, which accelerates the growth of the instability. Continuing the evolution further, we see the formation of two generations of satellites, e.g., small spherical beads joined by thin tubes, closely resembling the late stages of unstable strings and ultra-spinning BHs. Our numerics have allowed us to observe the onset of a third generation, in which all string segments present in the second generation, develop their own local GL instability. Note that in $7D$, the critical value for the width over length ratio of strings which are GL unstable is $r_{\text{GL},7D} \equiv \text{width}/\text{length} \approx 0.5$. We have explicitly

checked that the string segments present in our first and second generation are well below this value.

In Fig 4 we show the last time slice in our $7D$ simulation, where we overlay contours of the normalized Kretschmann scalar (3.1) computed at certain $\chi = \chi_0$ surfaces. As the top inset shows, the fact that the contour $\tilde{K}|_{\chi_0=0.6} = 1$ agrees very well with the $\chi = 0.6$ contour, indicates that the neck-like regions of the geometry are essentially described by stationary black strings of thickness $W(\chi_0 = 0.6)$. Furthermore, this implies that the $\chi = 0.6$ contours accurately track the horizon on the string-like regions of the geometry. Finally, the Kretschmann curvature scalar becomes very large inside the $\chi_0 = 0.6$ contour (see Fig. 6 below), and rapidly grows in time as the neck’s proper width W shrinks to zero, with a rate about $\propto W^{-4}$, as also observed for black strings [7, 8], and Myers-Perry black holes [17]. On the other hand, in the lower inset in Fig. 4, we see that the $\tilde{K}|_{\chi_0=0.7} = \frac{5}{2}$ hypersurface agrees very well with the $\chi = 0.7$ contour, indicating that the latter tracks the horizon in the bulge regions, which in turn are well-described by quasi-static $7D$ Schwarzschild black holes. Moreover, in Fig. 5 we compare the $\chi = 0.6$ (in blue), $\chi = 0.5$ (in black) and the $\chi = 0.3$ (in red) contours for the $7D$ BH collision described above. The fact that they all come very close to each other in the string-like region is a consequence of the steep near horizon gradients found in large D , and supports the idea that any such constant χ contour is a good proxy for the AH in the neck regions.

We have confirmed that for our configurations, the curvature at the AH grows without bound at late times. To do so, in Fig. 6 we display the logarithm of (the absolute value of) the normalised Kretschmann scalar as defined in Eq. (3.1) below, choosing as normalization factor the proper thickness of the $\chi = 0.6$ contour on the thin neck of the geometry in Fig. 4. The black line in this plot indicates the $\chi = 0.6$ contour which, according to the previous discussion, should correspond to the location of the AH in the neck regions of the geometry. This figure clearly shows that $\tilde{K}|_{\chi_0=0.6}$ is very large inside the neck regions. Note however that $\tilde{K}|_{\chi_0=0.6}$ does not diverge; the reason is that in the $(1 + \log)$ -slicing gauge that we use, the spatial hypersurfaces approach the physical singularity but they actually never touch it. Therefore, this figure shows that our spacelike hypersurfaces behave exactly as one would expect in the moving-puncture gauge.

4.1.2 Gravitational radiation

In this subsection we consider the gravitational waves emitted during the evolution of the system in $D = 7$, from the initial collision until well into the non-linear evolution of the GL instability. We have relegated the technical details of gravitational wave extraction in $7D$ to Appendix B.

We display the results for gravitational waves extracted for $D = 7$ in Fig. 7. In this figure, the small oscillations around $t - t_{\text{merger}} \lesssim 20$ are due to the initial constraint violations from superposing the two MP BHs and, hence, are discarded as unphysical. We observe that the first physical peak of radiation in the various modes appears at $t - t_{\text{merger}} \sim 30$, corresponding to the “collision” of the two BHs, when a common enveloping horizon first forms. As shown in the second panel in Fig 1, this common horizon is dumbbell shaped. Furthermore, this resulting BH is rotating since it acquires part of the total

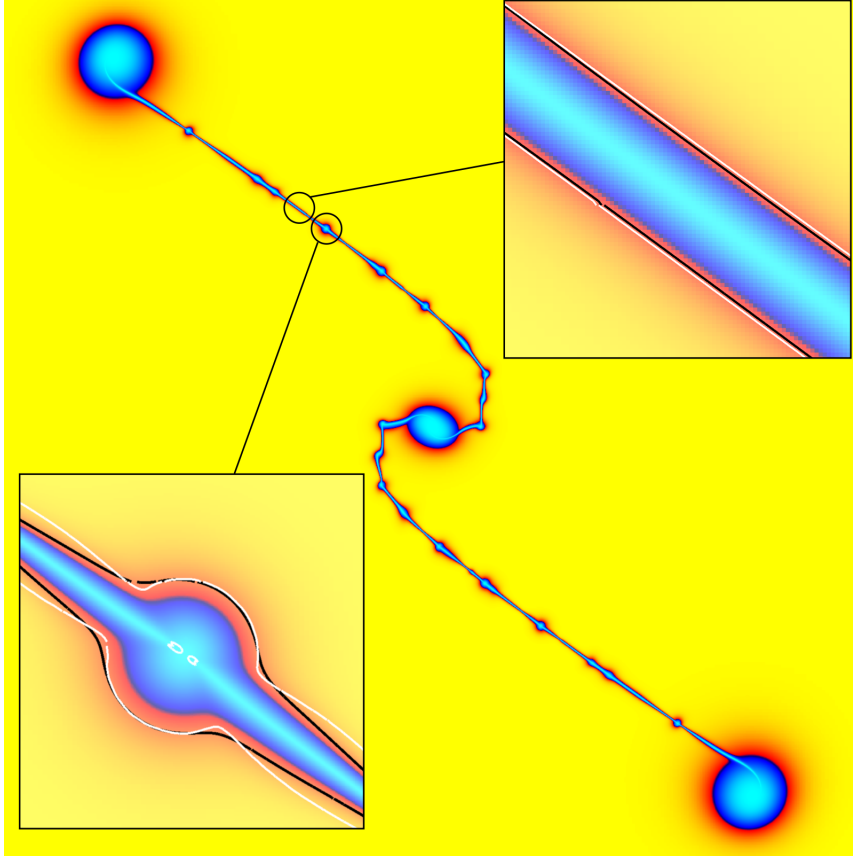


Figure 4: Last time slice shown in Fig 1 for the 7D collision at $\Delta t = 32.75$. We zoom into two different regions of the thinnest part of the geometry. In the string-like region (upper right inset) we show the $\chi = 0.6$ contour as a black line, and the $\tilde{K}|_{\chi_0=0.6} = 1$ contour in white. In the region near a satellite (lower left inset) we show the contours $\chi = 0.7$ in black and the $\tilde{K}|_{\chi_0=0.7} = 5/2$ contour in white. The fact that these contours are in very good agreement indicates that the contours of $\chi = 0.6, 0.7$ track the horizons of string-like and spherical-like portions of the geometry respectively. Furthermore, the unnormalized Kretschmann scalar diverges $\propto W^{-4}$, where W is the proper width of the neck-like regions of the geometry.

angular momentum of the initial state. At some point, which depends on the total initial angular momentum (and the number of dimensions D), the arms of the BH stop rotating and the necks connecting the two bulges to central BH start expanding, producing a second radiation peak; in the $D = 7$ example of Fig. 7, this second peak of radiation is visible at around $t - t_{\text{merger}} = 37.5$. It turns out that this second peak of radiation has the largest amplitude. We confirm this picture with a simple model in Appendix C.

We can compute the energy loss $\frac{dE}{dt}$ from the matrix of Weyl scalars according to the formula [36],

$$\frac{dE}{dt} = - \lim_{r \rightarrow \infty} \frac{r^{d-2}}{8\pi} \int_{S^{d-2}} \left(\int_{-\infty}^u \Omega'_{AB}(\hat{u}, r, x) d\hat{u} \right)^2 d\omega. \quad (4.1)$$



Figure 5: Comparison of the $\chi = 0.6$ (in blue), $\chi = 0.5$ (in black) and $\chi = 0.3$ (in red) contours for the the $7D$ BH collision. The $\chi = 0.6$ contour tracks the AH near the neck regions. The key features of the AH are captured by all these contours; in particular, in the neck regions they are very close to each other. This effect becomes more pronounced the larger D is.

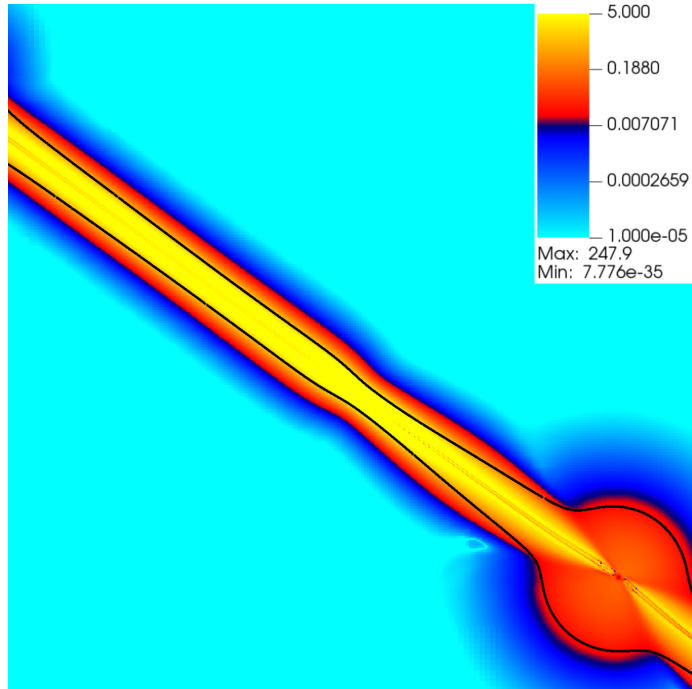


Figure 6: Logarithm of the absolute value of the normalized Kretschmann scalar $\tilde{K}|_{\chi_0=0.6}$ (as defined in the main text) for the last time slice of our $7D$ simulation. Note that this quantity spans several orders of magnitude between the $\chi = 0.6$ contour (black solid line) and the regions far away from it.

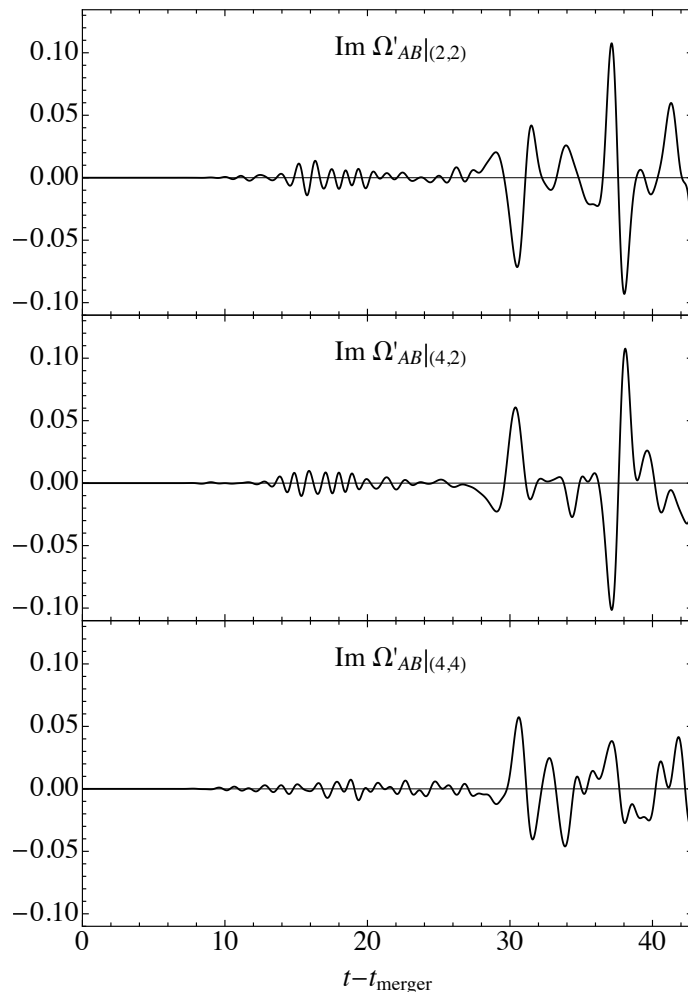


Figure 7: Imaginary part of the projection of the matrix of Weyl scalars Ω'_{AB} onto the harmonics $(\ell_5, m) = (2, 2), (4, 2), (4, 4)$ for the collision in $D = 7$. In this plot, the extraction was done at a radius $R = 30$ from the center of the grid. The first peak is observed at $t - t_{\text{merger}} \sim 30$, corresponding to the initial collision of the two BHs; the oscillations observed before this time are due to the constraint violations in the initial data and initial gauge adjustment. Two large peaks are observed in the $(2, 2)$ and $(4, 2)$ modes at around $t - t_{\text{merger}} \sim 37.5$. This corresponds to the time when the dumbbell-shaped horizon stops rotating and starts expanding. Beyond this point, whilst the gravitational wave signal continues to develop new features corresponding to the onset and further evolution of the local GL instability in the neck regions, their amplitude is never as large as that of these two initial peaks. Consequently, the energy loss in absolute value decreases.

where $d\omega$ is the volume element on the S^{d-2} . We display our results for the energy loss in $D = 7$ collision in Fig. 8. From this figure it follows that up until and including the second peak of radiation, the total radiated energy is about 0.01% of the Arnowitt-Deser-Misner (ADM) mass, which is very small. We expect that the radiation emitted at later

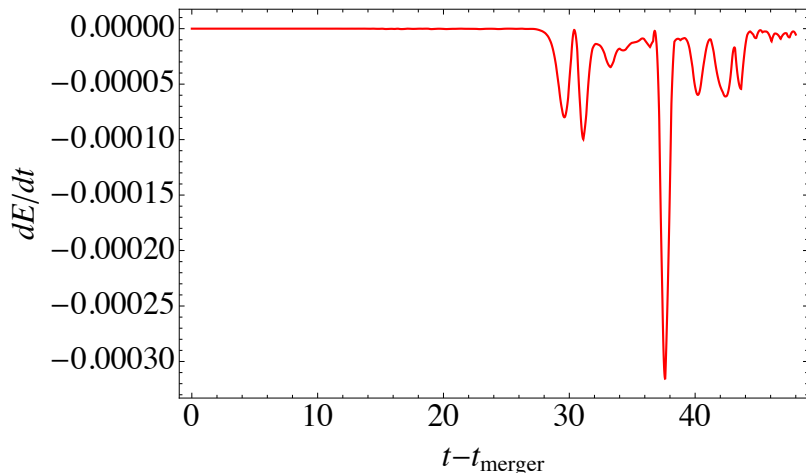


Figure 8: Energy loss for our $7D$ simulation as computed at a radius $R = 30$ from the merger point. The large peak at $t - t_{\text{merger}} \sim 37.5$ is produced when the dumbbell-shaped BH stops rotating and starts expanding.

stages to amount to an even smaller fraction, since the dynamics of the outer blobs is quasi-stationary and the GL cascade taking place in the neck regions of the AH produces very little radiation. The reason is that the mass contained in these highly dynamical regions is decreasingly small (Ref. [18] reports that less than 5% of the total ADM mass is radiated during the last stage of GL in the $6D$ evolution of ultraspinning BHs), so while higher modes will be excited, their amplitudes will be decreasing in time. We discuss this issue further in Appendix D, where we provide a crude upper bound on the total energy radiated.

In summary, we have shown that the effects of the gravitational radiation are sufficiently suppressed in $D \geq 7$. In the following subsection we will show that those effects are also suppressed in $D = 6$. Therefore, we conclude that there is no mechanism to stop the neck regions to reach zero thickness in finite time. Therefore, the violation of the WCC in BH collisions in $D \geq 6$ is inevitable provided that the initial total angular momentum of the system is sufficiently large.

4.2 $D = 6$

In this subsection we discuss the results that we have obtained in $D = 6$. As mentioned above, our results are qualitatively similar to the $D = 7$ case and hence we will be rather brief to avoid repetition. In summary, in the $D = 6$ case we also see strong evidence for the pinching off of the horizon in finite asymptotic time and hence the violation of the WCC.

We have run two high resolution simulations in cubic domains of size $L = 64$, with collision parameters $\{v = 0.5, a = 0.6, b = 2.5\}$, $\{v = 0.45, a = 0.7, b = 2.5\}$, respectively. Note that both of these values of a are well within the stability regime for rotating MP BHs $a_{\text{max}} = 0.73$ [15]. In this case we did not carry out the extraction of gravitational waves

due to a lack of computational resources, but we expect the waveforms to be qualitatively similar to the $D = 7$ case.

In Figs. 9, 10 we show representative snapshots of the conformal factor χ on the $z = 0$ plane. In the simulation shown in Fig. 9, the formation of the first generation of satellites is clear, and we observe that the dynamics closely resemble the $7D$ case. The critical dimensionless ratio for the GL instability in this dimension is $r_{\text{GL},6D} \equiv \text{width/length} \approx 0.4$. Estimating this value for $t = 13.6$ in Fig. 9, we find that $r_{\text{GL}} \approx 0.02$, showing that this string is well in the unstable regime. In the dynamics that follow, we again observe the appearance of the central rotating blob, joined to the outer blobs by thin strings. Our computational resources did not allow us to reach the same stage for the simulation in Fig. 10. However, we do observe a rapid thinning of the neck regions, which should lead to the development of the GL instability as in the previous cases. In particular, for $t = 15.0$ in Fig. 10 we estimate for $r_{\text{GL}} \approx 0.04$, so the strings are unstable.

As emphasised in the main text, no fine tuning is required to find configurations such as these in which the neck thins and the GL instability is triggered. The observed effects are therefore generic and not due any fine tuning.

5 Discussion

By means of numerical GR simulations, we have been able to provide evidence for the generic violation of the WCC conjecture in BH collisions $D = 6, 7$ spacetime dimensions. The driving mechanism is the GL instability, and the dynamics unfold in close parallel to other known cases of horizon pinching off. We have observed the formation of two generations of satellites and the beginning of a third one, which further improves our understanding of the dynamical process. We have extracted the gravitational waves emitted by the binaries, showing that there is a second peak of radiation which surpasses the initial burst due to the merger. After this second peak, we expect the emission of radiation to be small, paving the way for the GL instability to break the horizon. Since radiation is further suppressed in higher dimensions, our results strongly indicate that the violation of WCC we have identified is present in all $D \geq 6$.

It is remarkable that the large D effective theory [37–39], out of which the arguments for this mechanism were originally drawn [19, 20], is able to capture the qualitative dynamics so well. In hindsight, perhaps the main reason for its success in predicting the violation of WCC is the relatively small role that radiation plays already in $6D$.

As in all other known cases of WCC violation by fragmentation of horizons, the regions which we expect to become Planckian are “small” at least with respect to the size defined by the geometry of the apparent horizon. In the language of [40], they correspond to mild violations of WCC, which means that any suitable quantum resolution (analogue of the evaporation of a droplet in hydrodynamics) will have a small effect on the subsequent (classical) dynamics. In this sense, although the more strict version of the WCC conjecture is violated (naked singularities do appear in the course of evolution), its spirit is salvaged (the lack of predictability that the violations entail is very small). Note that according to this discussion, the singularity becomes visible because the horizon becomes infinitely

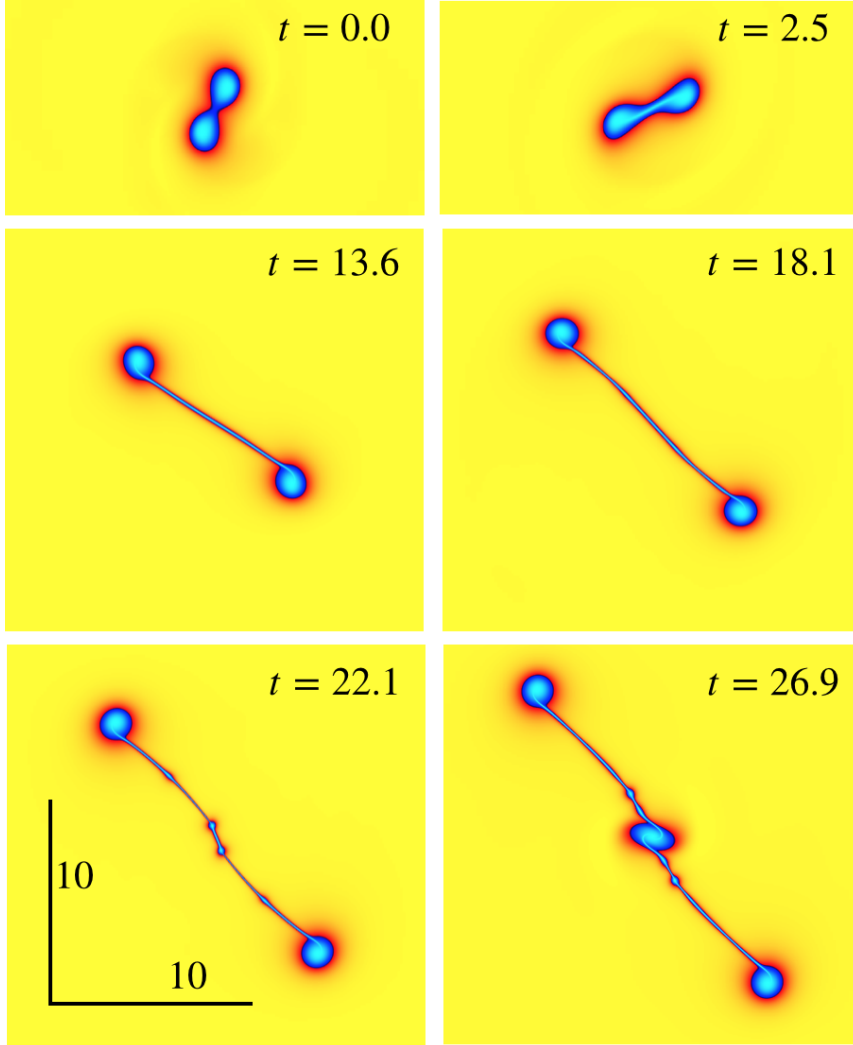


Figure 9: 6D-A evolution with $v = 0.5$, $a = 0.6$, $b = 2.5$.

thin. As in the previous works [7, 8, 16–18], while with our methods we cannot address the completeness of future null infinity, any horizon penetrating coordinates, such as those of moving-puncture gauge, are suitable to study the approach to the singularity. More specifically, we show that on the neck-like regions of the horizon the Kretschmann invariant diverges as the width W of the neck tends to zero; quantitative investigation furthermore reveals this blowup to be $\propto W^{-4}$. This is the same type of curvature blowup previously observed in black strings [7, 8] and in ultraspinning Myers-Perry black holes [17], which further supports the fact that underlying mechanism of approach to the singularity is the same in all these systems. Therefore, in finite time, asymptotic observers will have access to regions of arbitrarily large curvature, thus violating at least in spirit the WCC.

An interesting technical point which we have not addressed here is the derivation of the location of the apparent horizon from first principles. As discussed above, this requires parametrizing the shape of a reference surface, which is challenging in scenarios like ours

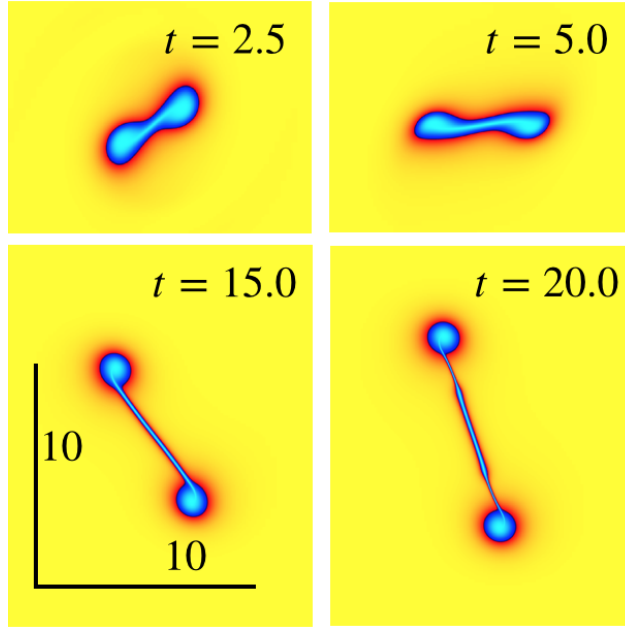


Figure 10: 6D-B evolution with $v = 0.45$, $a = 0.7$, $b = 2.5$.

where spatial modulation is constantly changing the shape of the horizon. Obtaining the apparent horizon in this way would allow us to accurately study entropy production. We leave these interesting issues for future research.

Acknowledgments

We thank Roberto Emparan for many insightful discussions. Our special thanks are for the entire GRChombo collaboration (www.grchombo.org) for their help and support. TA is supported by the ERC Advanced Grant GravBHs-692951. He also thanks QMUL for the hospitality during the early stages of this project. PF is supported by the European Research Council Grant No. ERC-2014-StG 639022-NewNGR, by a Royal Society University Research Fellowship (Grant No. UF140319 and URF\R\201026) and by a Royal Society Enhancement Award (Grant No. RGF\EA\180260). US acknowledges support from the European Union’s H2020 ERC Consolidator Grant “Matter and strong-field gravity: new frontiers in Einstein’s theory” Grant No. MaGRaTh646597, the STFC Consolidator Grant No. ST/P000673/1, and the GWverse COST Action Grant No. CA16104, “Black holes, gravitational waves and fundamental physics”. The simulations presented here were done on the MareNostrum4 cluster at the Barcelona Supercomputing Centre (Grant No. FI-2020-2-0011 and FI-2020-2-0016), the SDSC Comet and TACC Stampede2 clusters through NSF-XSEDE Grant No. PHY-090003, and the Cambridge Service for Data Driven Discovery (CSD3), part of which is operated by the University of Cambridge Research Computing on behalf of the STFC DiRAC HPC Facility (www.dirac.ac.uk). The DiRAC component of CSD3 was funded by BEIS capital funding via STFC capital grants ST/P002307/1 and

ST/R002452/1 and STFC operations grant ST/R00689X/1. DiRAC is part of the National e-Infrastructure.

A Initial data

We begin with a single, un-boosted MP BH with mass and rotation parameters μ , a . We write the metric as

$$g_{\mu\nu} = \eta_{\mu\nu} + f(\mathbf{x}) k_\mu k_\nu, \quad (\text{A.1})$$

where η is the Minkowski metric, f is a function of the space-time coordinates \mathbf{x} and k^μ is a null vector. For D even, the metric in Kerr-Schild form for a single BH is given by (A.1) with

$$f = \frac{\mu r}{\Pi(r)F(r, x^i)}, \quad (\text{A.2})$$

$$\Pi(r) = \Pi_i^{s(D)}(r^2 + a_i^2), \quad (\text{A.3})$$

$$F = 1 - \sum_{i=1}^{s(D)} \frac{a_i^2(X_i^2 + Y_i^2)}{(r^2 + a_i^2)}, \quad (\text{A.4})$$

$$k = dt + \sum_{i=1}^{s(D)} \frac{\{r(X_i dX_i + Y_i dY_i) + a_i(X_i dY_i - X_i dY_i)\}}{r^2 + a_i^2} + \frac{z dz}{r}, \quad (\text{A.5})$$

where $k = k_\mu dx^\mu$, $s(D) = (D - 2)/2$, and X_i, Y_i denote subsets of the coordinates that specify the rotation planes; they will be specified explicitly below. The index i runs from $1 \dots (D - 2)/2$, and corresponds to the number of possible rotation planes, in such a way that a non-vanishing a_i adds rotation on the axis orthogonal to (X_i, Y_i) . We explicitly display the sum over i to emphasise that there is no extra summation of repeated indices. The quantity denoted by r is not an independent coordinate, but can be expressed in terms of the X_i, Y_i by means of the condition $k_\mu k_\nu \eta^{\mu\nu} = 0$. In order to implement the modified cartoon method in $D = 6$, we choose $a_i = (a, 0)$, $X_i = (x, w_1)$, $Y_i = (y, w_2)$ with w_1, w_2 being isometric directions. This gives the BH rotation along the z -axis. Finally, we use a translation $(x', y') = (x - x_0, y - y_0)$ and a Lorentz boost along x ,

$$t'' = tc_\eta + x' s_\eta, \quad x'' = -ts_\eta + x' c_\eta \quad (\text{A.6})$$

with $c_\eta = \cosh \eta$, $s_\eta = \sinh \eta$ and $\cosh \eta = (1 - v^2)^{-1/2}$.

For odd D , we have Eqs. (A.2)-(A.4) along with

$$k = dt + \sum_{i=1}^{s(D)} \frac{\{r(X_i dX_i + Y_i dY_i) + a_i(X_i dY_i - X_i dY_i)\}}{r^2 + a_i^2} \quad (\text{A.7})$$

and now the number of rotation planes is $s(D) = (D - 1)/2$. To implement the cartoon method in $D = 7$, we choose $a_i = (a, 0, 0)$, and $X_i = (x, z, w_1)$, $Y_i = (y, w_2, w_3)$, where

(w_1, w_2, w_3) parametrize the isometric directions. This gives the BH rotation along the z -axis.

The mass and angular momentum for a single spinning BH are given by

$$M = \frac{(D-2)\Omega_{D-2}}{16\pi G}\mu, \quad J = \frac{2}{(D-2)}Ma, \quad (\text{A.8})$$

where

$$\Omega_{D-2} = \frac{2\pi^{(D-1)/2}}{\Gamma[(D-1)/2]}. \quad (\text{A.9})$$

B Gravitational waves in 7D

To extract the gravitational waves in higher dimensions, we have to project the matrix of Weyl scalars $\Omega'_{(A)(B)}$ computed on a certain orthonormal basis onto the basis of spherical harmonics $Y_{\ell\dots}^{(A)(B)}$ according to [36]:

$$\Omega'_{\ell\dots} = \lim_{r \rightarrow \infty} r^{(D-2)/2} \int d\Omega_{(n)} Y_{\ell\dots}^{(A)(B)} * \Omega'_{(A)(B)}. \quad (\text{B.1})$$

Here $\ell\dots$ denotes the set of quantum numbers of the spherical harmonics and $d\Omega_{(n)}$ is the volume element of the n -sphere; in our case, in $7D$ $\ell\dots = (\ell_5, m)$ and in $6D$, $\ell\dots = (\ell_4, m)$.

As is customary in numerical relativity, in order to carry out the gravitational wave extraction, we have used a finite computational domain of size $L = 256$, adding up to eleven levels in order to achieve equal resolutions at the horizons of the BHs as compared to the runs with $L = 64$. We have extracted the waves at radii $R = 25.0, 27.5, 30.0$ and observed the expected linear behaviour: all three wave forms match in all channels after the corresponding time shifts.

We now describe our basis for the tensor spherical harmonics on the S^5 . The relevant tensor harmonics on the S^4 needed for the analogous computation of the gravitational waves in the $6D$ collisions can be found in Ref. [18].

It is convenient to write the metric on the S^5 at infinity such that it has a manifest $SO(4)$ symmetry and one of its $U(1)$'s is aligned with the $U(1)$ on the rotation plane of the incoming MP BHs:

$$ds^2 = d\chi^2 + \sin^2 \chi d\phi^2 + \cos^2 \chi d\Omega_{(3)}^2, \quad (\text{B.2})$$

where $d\Omega_{(3)}^2$ is the metric on the unit S^3 .³ As shown in Ref. [18], due to the symmetries of the spacetime, the gravitational wave signal is contained in the scalar derived tensor harmonics. Given the form of the metric (B.2), a convenient basis for the scalar harmonics on the S^5 is

$$\begin{aligned} \mathbb{Y}^{\ell_5, m, \ell_3, \dots} &= N e^{im\phi} (\sin \chi)^{|m|} (\cos \chi)^{\ell_3} \mathbb{Y}^{\ell_3 \dots} \\ &\times {}_2F_1\left(\ell_3 + |m| - k, k + \frac{3}{2}, \ell_3 + \frac{2}{2}; \cos^2 \chi\right), \end{aligned} \quad (\text{B.3})$$

³In this appendix we use χ to denote the polar angle on the S^5 ; it should not be confused with the conformal factor of the induced metric on the spacelike hypersurfaces.

where ${}_2F_1$ is a hypergeometric function, N is a normalization factor, k is a non-negative integer and $\mathbb{Y}^{\ell_3 \dots}$ are the scalar harmonics on the S^3 , so that $\Delta_{S^3} \mathbb{Y}^{\ell_3 \dots} = -\ell_3(\ell_3 + 2) \mathbb{Y}^{\ell_3 \dots}$; the dots in $\mathbb{Y}^{\ell_3 \dots}$ denote the remaining labels for the quantum numbers of the harmonics. Regularity of the harmonics implies

$$\ell_5 = 2k - (\ell_3 + |m|). \quad (\text{B.4})$$

Since the spacetimes that we consider in this paper preserve a round S^3 inside the S^5 , to extract the gravitational waves we only need to consider harmonics on the S^5 that also preserve a round S^3 . Therefore, from now on, in (B.3) we will consider harmonics with $\ell_3 = 0$ and hence we can uniquely label them with only two quantum numbers, (ℓ_5, m) .

Scalar derived traceless tensor harmonics on the n -sphere can be constructed from the scalar harmonics by⁴

$$\begin{aligned} \mathbb{S}_{ab}^{\ell_n, \dots, \ell_1} &= \frac{\sqrt{n}}{\sqrt{(n-1)(\ell_n-1)(\ell_n+n)}} \\ &\times \left(\nabla_a \mathbb{S}_b^{\ell_n, \dots, \ell_1} + \frac{\sqrt{\ell_n(\ell_n+n-1)}}{n} g_{ab} \mathbb{S}^{\ell_n, \dots, \ell_1} \right), \end{aligned} \quad (\text{B.5})$$

where $\mathbb{S}_a^{\ell_n, \dots, \ell_1} \equiv \frac{1}{\sqrt{\ell_n(\ell_n+n-1)}} \nabla_a \mathbb{S}^{\ell_n, \dots, \ell_1}$ are the scalar derived vector harmonics, and g_{ab} is the metric on the unit S^n . The coefficients are chosen so that the scalar derived tensor harmonics are suitably normalized:

$$\int_{S^n} g^{ac} g^{bd} \mathbb{S}_{ab}^{\ell_n, \dots, \ell_1} \mathbb{S}_{cd}^{\ell'_n, \dots, \ell'_1} = \delta_{\ell_n \ell'_n \dots \ell_1 \ell'_1}. \quad (\text{B.6})$$

To do the extraction, we need to compute the tensor harmonics on the S^5 in a certain basis of angular vectors. For the metric in (B.2), we choose the obvious basis,

$$m_{(1)} = \frac{\partial}{\partial \chi}, \quad m_{(2)} = \frac{1}{\sin \chi} \frac{\partial}{\partial \phi}, \quad m_{(i)} = \frac{1}{\cos \chi} \hat{m}_{(i)}, \quad (\text{B.7})$$

where $\hat{m}_{(i)}$, $i = 1, 2, 3$ are a basis of angular (unit) vectors on the S^3 .

After these preliminaries, we are now ready to list the non-vanishing components of the scalar derived tensor harmonics on the S^5 that we have used to extract the gravitational waves:

- $(\ell_5, m) = (2, 0)$:

$$\begin{aligned} \mathbb{S}_{11}^{(2,0)} &= \frac{1}{\pi^{3/2}} \sqrt{\frac{3}{70}} [2 \cos(2\chi) + 1], \\ \mathbb{S}_{22}^{(2,0)} &= -\frac{1}{\pi^{3/2}} \sqrt{\frac{3}{70}} [\cos^2(\chi) - 4], \\ \mathbb{S}_{ij}^{(2,0)} &= -\frac{\delta_{ij}}{2\pi^{3/2}} \sqrt{\frac{3}{70}} [\cos(2\chi) + 3]. \end{aligned} \quad (\text{B.8})$$

⁴There is a typo in the analogous formula for the scalar derived tensor harmonics in [18], which we correct here.

- $(\ell_5, m) = (2, 2)$:

$$\begin{aligned}
\mathbb{S}_{11}^{(2,2)} &= \frac{1}{\sqrt{70}\pi^{3/2}} e^{2i\phi} [2 \cos(2\chi) + 3], \\
\mathbb{S}_{12}^{(2,2)} &= \frac{i}{\pi^{3/2}} \sqrt{\frac{5}{14}} e^{2i\phi} \cos(\chi), \\
\mathbb{S}_{22}^{(2,2)} &= -\frac{1}{2\sqrt{70}\pi^{3/2}} e^{2i\phi} [\cos(2\chi) + 9], \\
\mathbb{S}_{ij}^{(2,2)} &= \frac{\delta_{ij}}{\sqrt{70}\pi^{3/2}} e^{2i\phi} \sin^2(\chi).
\end{aligned} \tag{B.9}$$

- $(\ell_5, m) = (4, 0)$:

$$\begin{aligned}
\mathbb{S}_{11}^{(4,0)} &= -\frac{1}{2\sqrt{10}\pi^{3/2}} [\cos(2\chi) + 5 \cos(4\chi) - 2], \\
\mathbb{S}_{22}^{(4,0)} &= \frac{1}{8\sqrt{10}\pi^{3/2}} [-24 \cos(2\chi) + 5 \cos(4\chi) + 3], \\
\mathbb{S}_{ij}^{(4,0)} &= \frac{\delta_{ij}}{24\sqrt{10}\pi^{3/2}} [28 \cos(2\chi) + 15 \cos(4\chi) - 11].
\end{aligned} \tag{B.10}$$

- $(\ell_5, m) = (4, 2)$:

$$\begin{aligned}
\mathbb{S}_{11}^{(4,2)} &= -\frac{1}{4\sqrt{5}\pi^{3/2}} e^{2i\phi} [2 \cos(2\chi) + 5 \cos(4\chi) - 2], \\
\mathbb{S}_{12}^{(4,2)} &= \frac{i\sqrt{5}}{16\pi^{3/2}} e^{2i\phi} [\cos(\chi) - 5 \cos(3\chi)], \\
\mathbb{S}_{22}^{(4,2)} &= \frac{1}{16\sqrt{5}\pi^{3/2}} e^{2i\phi} [2 \cos(2\chi) + 5 \cos(4\chi) + 13], \\
\mathbb{S}_{ij}^{(4,2)} &= -\frac{\delta_{ij}}{4\sqrt{5}\pi^{3/2}} e^{2i\phi} \sin^2(\chi) [5 \cos(2\chi) + 6]
\end{aligned} \tag{B.11}$$

- $(\ell_5, m) = (4, 4)$:

$$\begin{aligned}
\mathbb{S}_{11}^{(4,4)} &= \frac{1}{2\sqrt{2}\pi^{3/2}} e^{4i\phi} \sin^2(\chi) [2 \cos(2\chi) + 3], \\
\mathbb{S}_{12}^{(4,4)} &= \frac{5i}{2\sqrt{2}\pi^{3/2}} e^{4i\phi} \sin^2(\chi) \cos(\chi), \\
\mathbb{S}_{22}^{(4,4)} &= -\frac{1}{4\sqrt{2}\pi^{3/2}} e^{4i\phi} \sin^2(\chi) [\cos(2\chi) + 9], \\
\mathbb{S}_{ij}^{(4,4)} &= \frac{1}{2\sqrt{2}\pi^{3/2}} e^{4i\phi} \sin^4(\chi).
\end{aligned} \tag{B.12}$$

The harmonics with negative m can be obtained from the ones listed above by complex conjugation.

Finally, to do the extraction we compute the components of the matrix of Weyl scalars $\Omega'_{(A)(B)}$ in a certain orthonormal basis. We construct the latter starting from

$$\begin{aligned}
m_{(1)} &= x \partial_x + y \partial_y + z \partial_z, \\
m_{(2)} &= x z \partial_x + y z \partial_y - (x^2 + y^2) \partial_z, \\
m_{(3)} &= -y \partial_x + x \partial_y,
\end{aligned} \tag{B.13}$$

and carrying out a standard Gram-Schmidt orthonormalization.⁵ The unit vectors on the transverse sphere direction are simply given by

$$m_{(\hat{i})} = \frac{1}{\sqrt{\gamma_{ww}}} \partial_{w_i}. \quad (\text{B.14})$$

One can show that, asymptotically, the angular basis vectors obtained from (B.13) are aligned with (B.7).

C Radiation peak due to separation

In order to elucidate the origin of the second peak that we observe in the pattern on gravitational radiation, we consider a simple model for a higher dimensional binary and use the quadrupole formula of [41]. Since a general expression is only available for even dimensions, we consider the case $D = 6$ which we expect will best capture the qualitative features of our setting.

The corresponding quadrupole formula for even D can be written as [41]

$$\frac{dE}{dt} = P(D) \left[(D-1) \partial_t^{\frac{D+2}{2}} M_{ij}(t) \partial_t^{\frac{D+2}{2}} M_{ij}(t) - \left| \partial_t^{\frac{D+2}{2}} M_{ii}(t) \right|^2 \right]. \quad (\text{C.1})$$

where the prefactor is given by

$$P(D) = \frac{2^{2-D} (D-3) D}{\pi^{\frac{D-5}{2}} \Gamma\left[\frac{D-1}{2}\right] (D^2-1) (D-2)} G, \quad (\text{C.2})$$

and

$$M^{ij} = \int d^{D-1}x T^{00}(t, x) x^i x^j. \quad (\text{C.3})$$

In addition, [20] provided an expression for the emission of angular momentum in even dimensions, which in our case reduces to

$$\frac{dJ^{ij}}{dt} = \frac{4(D^2-1)}{D+2} P(D) \left[\partial_t^{\frac{D+2}{2}} Q^{[i} \partial_t^{\frac{D}{2}} Q^{j]} \right], \quad (\text{C.4})$$

where

$$Q^{ij} = M^{ij} - \frac{1}{D-1} \delta_{ij} M_{kk}. \quad (\text{C.5})$$

In order to evaluate these expressions, we make the assumption that the energy distribution T^{00} is simply a delta function with support on two point particles that follow a trajectory on a two-dimensional plane. We parametrize the trajectory in polar coordinates $x_1(t) = \rho(t) \cos \theta(t)$, $x_2(t) = \rho(t) \sin \theta(t)$. For concreteness, we consider a circular binary which slows down and separates along a straight line. This captures some of the qualitative features we observe in our simulations after merger. We show the profiles we have chosen for ρ and θ in Fig 11 (top) while the obtained pattern for energy and angular momentum loss is depicted on Fig 11 (bottom). At early times we observe a sinusoidal pattern for

⁵Note that this basis differs from the one used in [18]. The reason is explained below.

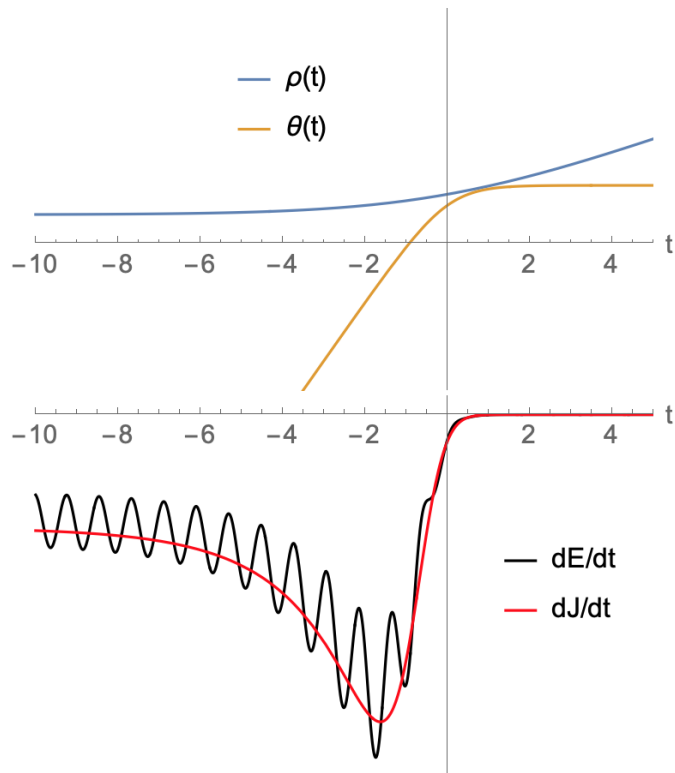


Figure 11: *Top:* Trajectory for a binary which starts in a circular orbit and experiences a slow down and separation. (*Bottom:*) Energy and angular momentum loss as computed from the quadrupole formulae (C.1), (C.4) in $6D$.

energy radiation characteristic of a circular binary. Interestingly, the later slow down and separation leads to a relatively sharp peak, which resembles the second radiation peak we observe in Fig 8. We also observe that the radiated angular momentum follows the pattern of the radiated energy averaged over the orbits.

D Radiated energy and angular momentum

We approximate the total initial and final mass and angular momentum according to

$$M_i = 2\gamma_i m_i, \quad (\text{D.1})$$

$$M_f = 2\gamma_f m_f + m_{\text{central}} + 2m_{\text{string}}, \quad (\text{D.2})$$

$$J_i = \gamma_i m_i \left[b_i v_i + 2 \frac{2}{D-2} a_i \right], \quad (\text{D.3})$$

$$J_f = \left[\gamma_f m_f b_f v_f + \frac{2}{D-2} m_{\text{central}} a_{\text{central}} \right]. \quad (\text{D.4})$$

Here m_i is the mass of the BHs in the initial state, with velocities v_i , spins a_i and impact parameter b_i – defined as the distance between the center of the BHs and the plane along

which the binary is reflection symmetric, i.e. $b_i = y_0$ in the notation of the main text –, m_f is the mass of the BHs at the extremes of the final dumbbell, which have velocities v_f and impact parameter b_f (we have checked that they do not have intrinsic spin), $m_{central}$, $a_{central}$ are the mass and spin of the central BH, and m_{string} is the mass of each of the strings joining the central and outer BHs.

We assume the BHs and strings involved in this calculation to be stationary, in which case we can compute their properties from Eq. (A.8) and (we set $G = 1$ henceforth)

$$M_{string} = \frac{(D-2)\Omega_{D-2}}{16\pi G} r_+ L. \quad (\text{D.5})$$

The initial parameters are given by (recall $\mu = 1$),

$$m_i = 3.1, \quad v_i = 0.5, \quad b_i = 2.2, \quad a_i = 0.7. \quad (\text{D.6})$$

For the final parameters, we can measure v_f and b_f by tracking the position of the outgoing blobs, and extracting the metric components in the region of the corresponding blobs. We find

$$v_f \approx 0.3, \quad b_f \approx 4.26. \quad (\text{D.7})$$

We see that the outgoing BHs do not rotate, so they can be approximated Schwarzschild BHs. Their mass is then given by

$$m_f \approx 3.1. \quad (\text{D.8})$$

The mass and rotation parameter of the central blob can be estimated by computing $\Omega = \beta^\phi \approx 1.5$, $g_{\phi\phi} \approx 0.25$ and comparing this with the values for a MP BH. We obtain

$$m_{central} \approx 0.07, \quad J \approx 0.009, \quad a_{central} \approx 0.32. \quad (\text{D.9})$$

Collecting these results, we obtain

$$M_i \approx 7.1, \quad J_i \approx 5.9, \quad M_f \approx 6.6, \quad J_f \approx 4.2. \quad (\text{D.10})$$

Assuming that there could be an uncertainty of 10% in the values of m_f , v_f and b_f , we obtain that about $8_{-10}^{+10}\%$ of the total mass-energy and $30_{-25}^{+19}\%$ of the angular momentum are radiated.

E Numerical tests

In all of our simulations, we ensure that the region contained within the $\chi = 0.6$ contour is covered by at least 40 grid points. Unacceptably large constraint violations due to insufficient resolution lead to unphysical effects, such as a rapid swelling of the horizon.

In view of the very high computational resources needed for the simulations presented in this work (about 2M CPU hours per run), a standard convergence analysis with two additional simulations at higher resolution is prohibitively costly. In order to achieve a practical convergence study, we apply two steps that greatly reduce the expenses. First, we consider a quantity whose continuum limit is already known, namely the Hamiltonian

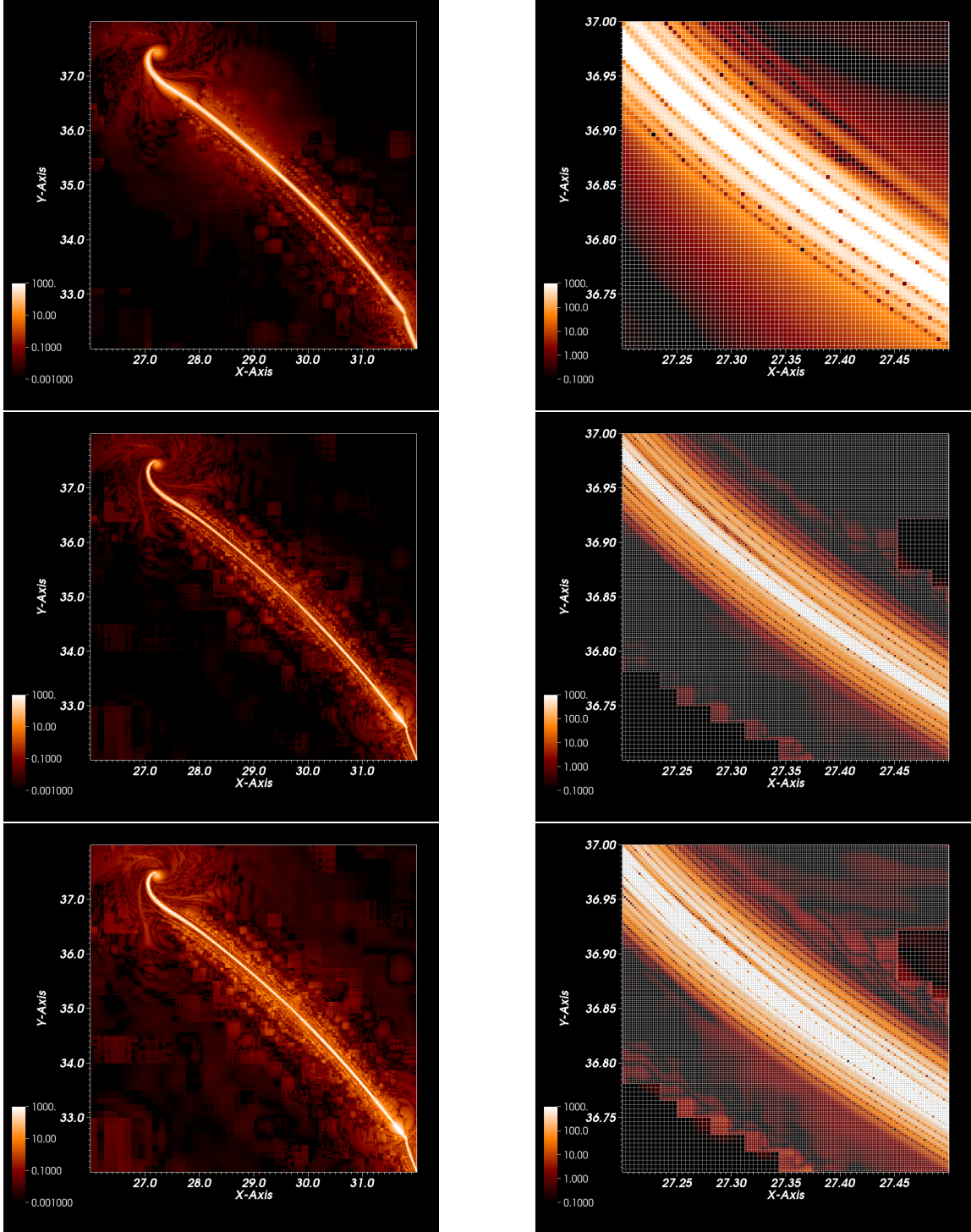


Figure 12: *Left column:* The Hamiltonian constraint for the 6D-A simulation in the xy plane at $t = 22$. The upper panel shows the constraint obtained using 8 refinement levels only. The constraint with an additional 9th level is shown in the center panel and, amplified by a factor $Q_2 = 4$ for second-order convergence, in the bottom panel. *Right column:* A zoom-in of each of the left panels shows the constraint in a smaller region around the string. Here, we also display the grid structure in the form of a gray mesh.

constraint. This reduces the number of required resolutions from three to two. Second, instead of repeating the entire simulation, we use the fact that the code dynamically adds resolution in the critical regions by adding extra refinement levels. More specifically, we have performed the later stages of the $6D$ -A simulation twice. In one case, the code adds, as instructed by the tagging criterion, an additional refinement level, the 9th level, that covers the black string region and the satellites. In the second case, we have disallowed the code from adding this level and instead let the simulation continue from its previous checkpoint with a mere 8 refinement levels. These two instances of our simulation enable us to analyse the dependence of the Hamiltonian constraint on resolution in the vicinity of the high curvature region. We note in this context that the constraint violations rapidly decrease in the outer regions of our computational domain, as expected from the rapid fall-off of gravity in higher-dimensional spacetimes.

In Fig. 12, we show the Hamiltonian constraint for the $6D$ -A simulation in the xy plane at $t = 22$. For better image quality, we display only the upper left half of the string in the left column of this figure; the lower right half is obtained from reflection across each panel's bottom right corner. Let us first compare the upper and center panels which are obtained using 8 and 9 levels, respectively. We clearly see that the string shaped region of large constraint violations is thicker for the lower resolution in the upper panel. The resulting larger constraint violations also extend into the outer regions as visible in the form of the cloud like structure surrounding the string, especially in the upper half. Both these effects are visibly reduced by the higher resolution around the string in the center panel, although at a small price: the additional refinement boundaries introduce some numerical noise visible in the form of the rectangular structures in the center panel.

In order to obtain a rough estimate of the convergence order, we show in the bottom left panel of Fig. 12 the higher resolution result amplified by a factor $Q_2 = 4$ as expected for second-order convergence, which is the dominant discretization order in the prologation operation. This amplification roughly widens the region of larger constraint violations in the bottom panel to a level comparable to the top panel. Note that we only expect this convergence in the immediate vicinity of the string, where extra refinement is present in the center and bottom panels.

In order to obtain a clearer illustration of the rate of convergence, we show in the right column of Fig. 12 the same result but now for a small region around the string, where we are now also able to display the grid structure. Again, the effect of the additional resolution near the string in the lower two panels is clearly perceptible. The comparable width of the string in the top and bottom panel furthermore indicates convergence commensurate with 2nd order around the string.

References

- [1] S. W. Hawking and R. Penrose, *The singularities of gravitational collapse and cosmology*, *Proc. Roy. Soc. Lond.* **A314** (1970) 529–548.
- [2] R. Penrose *Riv. Nuovo Cim.* **1** (1969) 252–276. [Gen. Rel. Grav.34,1141(2002)].

- [3] M. W. Choptuik, *Universality and scaling in gravitational collapse of a massless scalar field*, *Phys. Rev. Lett.* **70** (1993) 9–12.
- [4] R. Gregory and R. Laflamme *Phys. Rev. Lett.* **70** (1993) 2837–2840.
- [5] J. Eggers, *Universal pinching of 3d axisymmetric free-surface flow*, *Phys. Rev. Lett.* **71** (Nov, 1993) 3458–3460.
- [6] J. Eggers, *Nonlinear dynamics and breakup of free-surface flows*, *Rev. Mod. Phys.* **69** (Jul, 1997) 865–930.
- [7] L. Lehner and F. Pretorius *Phys. Rev. Lett.* **105** (2010) 101102.
- [8] L. Lehner and F. Pretorius, *Final State of Gregory-Laflamme Instability*, [1106.5184](#).
- [9] J. E. Santos and B. Way *Phys. Rev. Lett.* **114** (2015) 221101.
- [10] R. Emparan and R. C. Myers *JHEP* **09** (2003) 025.
- [11] O. J. C. Dias, P. Figueras, R. Monteiro, J. E. Santos and R. Emparan *Phys. Rev.* **D80** (2009) 111701.
- [12] O. J. C. Dias, P. Figueras, R. Monteiro, H. S. Reall and J. E. Santos *JHEP* **05** (2010) 076.
- [13] M. Shibata and H. Yoshino *Phys. Rev.* **D81** (2010) 021501.
- [14] M. Shibata and H. Yoshino *Phys. Rev.* **D81** (2010) 104035.
- [15] O. J. C. Dias, G. S. Hartnett and J. E. Santos *Class. Quant. Grav.* **31** (2014), no. 24 245011.
- [16] P. Figueras, M. Kunesch and S. Tunyasuvunakool, *End Point of Black Ring Instabilities and the Weak Cosmic Censorship Conjecture*, *Phys. Rev. Lett.* **116** (2016), no. 7 071102 [[1512.04532](#)].
- [17] P. Figueras, M. Kunesch, L. Lehner and S. Tunyasuvunakool, *End Point of the Ultraspinning Instability and Violation of Cosmic Censorship*, *Phys. Rev. Lett.* **118** (2017), no. 15 151103 [[1702.01755](#)].
- [18] H. Bantilan, P. Figueras, M. Kunesch and R. Panosso Macedo, *End point of nonaxisymmetric black hole instabilities in higher dimensions*, *Phys. Rev. D* **100** (2019), no. 8 086014 [[1906.10696](#)].
- [19] T. Andrade, R. Emparan, D. Licht and R. Luna, *Cosmic censorship violation in black hole collisions in higher dimensions*, *JHEP* **04** (2019) 121 [[1812.05017](#)].
- [20] T. Andrade, R. Emparan, D. Licht and R. Luna, *Black hole collisions, instabilities, and cosmic censorship violation at large D* , *JHEP* **09** (2019) 099 [[1908.03424](#)].
- [21] U. Sperhake, V. Cardoso, F. Pretorius, E. Berti and J. A. González, *The high-energy collision of two black holes*, *Phys. Rev. Lett.* **101** (2008) 161101. arXiv:0806.1738 [gr-qc].
- [22] U. Sperhake, W. Cook and D. Wang, *The high-energy collision of black holes in higher dimensions*, *Phys. Rev. D* **100** (2020), no. 10 104046 [[1909.02997](#)].
- [23] U. Sperhake, V. Cardoso, F. Pretorius, E. Berti, T. Hinderer and N. Yunes, *Cross section, final spin and zoom-whirl behavior in high-energy black hole collisions*, *Phys. Rev. Lett.* **103** (2009) 131102. arXiv:0907.1252 [gr-qc].
- [24] “GRChombo Youtube channel: Rotating black hole collision in 7d.” https://youtu.be/Ytqg9XX_4sM.

- [25] D. Alic, C. Bona-Casas, C. Bona, L. Rezzolla and C. Palenzuela *Phys. Rev.* **D85** (2012) 064040.
- [26] A. Weyhausen, S. Bernuzzi and D. Hilditch *Phys. Rev.* **D85** (2012) 024038.
- [27] F. Pretorius *Class. Quant. Grav.* **22** (2005) 425–452.
- [28] W. G. Cook, P. Figueras, M. Kunesch, U. Sperhake and S. Tunyasuvunakool *Int. J. Mod. Phys.* **D25** (2016), no. 09 1641013.
- [29] R. C. Myers and M. J. Perry, *Black Holes in Higher Dimensional Space-Times*, *Ann. Phys.* **172** (1986) 304.
- [30] U. Sperhake, *Binary black-hole evolutions of excision and puncture data*, *Phys. Rev. D* **76** (2007) 104015 [[gr-qc/0606079](#)].
- [31] W. G. Cook, D. Wang and U. Sperhake, *Orbiting black-hole binaries and apparent horizons in higher dimensions*, *Class. Quant. Grav.* **35** (2018), no. 23 235008 [[1808.05834](#)].
- [32] K. Clough, P. Figueras, H. Finkel, M. Kunesch, E. A. Lim and S. Tunyasuvunakool *Class. Quant. Grav.* **32** (2015), no. 24 245011.
- [33] M. Adams, P. Colella, D. Graves, J. Johnson, N. Keen, T. Ligocki, D. Martin, P. McCorquodale, D. Modiano, P. Schwartz, T. Sternberg and B. Van Straalen, *Chombo software package for amr applications - design document*, Tech. Rep. LBNL-6616E, Lawrence Berkeley National Laboratory, 2015.
- [34] D. Pook-Kolb, O. Birnholtz, B. Krishnan and E. Schnetter, *Existence and stability of marginally trapped surfaces in black-hole spacetimes*, *Phys. Rev. D* **99** (2019), no. 6 064005 [[1811.10405](#)].
- [35] D. Pook-Kolb, O. Birnholtz, B. Krishnan and E. Schnetter, *Self-intersecting marginally outer trapped surfaces*, *Phys. Rev. D* **100** (2019), no. 8 084044 [[1907.00683](#)].
- [36] M. Godazgar and H. S. Reall, *Peeling of the Weyl tensor and gravitational radiation in higher dimensions*, *Phys. Rev. D* **85** (2012) 084021 [[1201.4373](#)].
- [37] R. Emparan, T. Shiromizu, R. Suzuki, K. Tanabe and T. Tanaka, *Effective theory of Black Holes in the 1/D expansion*, *JHEP* **06** (2015) 159 [[1504.06489](#)].
- [38] R. Emparan, R. Suzuki and K. Tanabe, *Evolution and End Point of the Black String Instability: Large D Solution*, *Phys. Rev. Lett.* **115** (2015), no. 9 091102 [[1506.06772](#)].
- [39] R. Emparan, K. Izumi, R. Luna, R. Suzuki and K. Tanabe, *Hydro-elastic Complementarity in Black Branes at large D*, *JHEP* **06** (2016) 117 [[1602.05752](#)].
- [40] R. Emparan, *Predictivity lost, predictivity regained: a Miltonian cosmic censorship conjecture*, [2005.07389](#).
- [41] V. Cardoso, O. J. Dias and J. P. Lemos, *Gravitational radiation in D-dimensional space-times*, *Phys. Rev. D* **67** (2003) 064026 [[hep-th/0212168](#)].